

# Structural and magnetic studies on Mn-doped Ni–Zn ferrite nanoparticles

S. Ramesh<sup>1</sup> · B. Dhanalakshmi<sup>2</sup> · B. Chandra Sekhar<sup>3</sup> · P. S. V. Subba Rao<sup>2</sup> · B. Parvatheeswara Rao<sup>2</sup>

Received: 23 August 2016 / Accepted: 19 October 2016 / Published online: 26 October 2016  
© Springer-Verlag Berlin Heidelberg 2016

**Abstract** Ni–Zn ferrite nanoparticles with manganese substitutions,  $\text{Ni}_{0.4}\text{Zn}_{0.6-x}\text{Mn}_x\text{Fe}_2\text{O}_4$ , where  $x$  varies from 0.00 to 0.25 in steps of 0.05, were prepared using sol–gel autocombustion method. The resultant nanoparticles were analyzed using X-ray diffractometry, transmission electron microscopy, thermogravimetry and vibrating sample magnetometer measurements. X-ray diffraction patterns confirm single-phase cubic spinel structures with crystallite sizes in the range from 25.43 to 37.23 nm. Particle sizes obtained from transmission electron micrographs were also in good agreement with the crystallite sizes obtained from the X-ray data. Saturation magnetization and coercivity data for all the samples obtained from the corresponding M–H loops suggest a sinusoidal variations with Mn concentration ( $x$ ) implying that the substitution of Mn in the given nano-sized Ni–Zn ferrite system seems to have brought in a profound influence not only on the site preferences of other cations in the system but also in bringing about modifications in its own site preferences. The results are analyzed in terms of the compositional and structural modifications, and it was found that the observed magnetic variation was governed by the crystallite size and the corresponding change in cationic preferences in these materials.

## 1 Introduction

Ferrite nanoparticles are emerged as an important class of magnetic materials finding large number of applications in several fields including magnetic separation, biomedical and consumer electronics. Inexpensive raw materials, ease in synthesis and excellent magnetic performance make the ferrite nanoparticles attractive over their metal magnetic counterparts for these applications [1]. Further, the recent upsurge in the study of ferrites at nanoscales for power applications is mainly driven by the assumption of an enhanced structural and magnetic performance over their ceramic counterparts particularly in dealing with the limit due to domain wall resonance [2]. When the size of the ferrite nanoparticle is smaller than the critical size for multi-domain formation, the particle exists in a single-domain state and obviously, the domain wall resonance is avoided; thus, the material can work at higher frequencies. Also, recently, there has been enhanced interest in developing size-controlled magnetic nanoparticles, including ferrites, with different chemical compositions due to their increased scope for applications in targeted drug delivery, hyperthermia, magnetic resonance imaging and biosensing labels [3]. Nevertheless, considering the vast potential for ferrite nanoparticles to be used as elements in application systems, it is felt necessary to carry out more investigations on mixed ferrite nanoparticles.

The properties of ferrite nanoparticles strongly depend on the chemical composition as well as the method of synthesis. From a close survey of the literature on various synthesis methods for generation of nanoparticles, it can be mentioned on a consensus that the chemical methods often provide better homogeneity and greater uniformity in particle size and size distribution. The methods include coprecipitation [4], sol–gel [5], microemulsion [6],

✉ B. Dhanalakshmi  
deepthi0527@gmail.com

<sup>1</sup> School of Technology, GITAM University, Bengaluru, India

<sup>2</sup> Department of Physics, Andhra University,  
Visakhapatnam 530003, India

<sup>3</sup> Vignan's Institute of Engineering for Women,  
Visakhapatnam 530046, India

hydrothermal [7], etc. Though all these works produce useful properties with varied particle sizes independently, they are also inherited with some disadvantages such as use of expensive precursors, long synthesis times, tedious washing procedures, low yields, etc. However, sol–gel autocombustion method, which is evolved from a combination of both sol–gel and combustion processes, is one method that produces fully crystalline ferrite nanoparticles at low temperatures in larger yields using inexpensive raw materials with much ease in synthesis. Therefore, it is felt desirable to make use of this method for the synthesis of ferrite nanoparticles in the present work. Further, in order to find out the effect of compositional modifications, it is proposed to investigate a series of Ni–Zn ferrite compositions with Mn substitutions in this study. A study of this kind helps not only in arriving at required materials with desired physical and magnetic characteristics for applications mentioned above but also in understanding the mechanisms responsible for such structural and magnetic transformations in their evolution.

## 2 Experimental

Ni–Zn–Mn ferrite nanoparticles with the formulae,  $\text{Ni}_{0.4}\text{Zn}_{0.6-x}\text{Mn}_x\text{Fe}_2\text{O}_4$ , where  $x$  varies from 0.00 to 0.25 in steps of 0.05, have been prepared by sol–gel autocombustion method. For this purpose, analytical reagent grade nickel nitrate [ $\text{Ni}(\text{NO}_3)_2 \cdot 6\text{H}_2\text{O}$ ], zinc nitrate [ $\text{Zn}(\text{NO}_3)_2 \cdot 6\text{H}_2\text{O}$ ], manganese nitrate [ $\text{Mn}(\text{NO}_3)_2 \cdot 4\text{H}_2\text{O}$ ], iron nitrate [ $\text{Fe}(\text{NO}_3)_3 \cdot 9\text{H}_2\text{O}$ ], citric acid [ $\text{C}_6\text{H}_8\text{O}_7$ ] and ammonia were used as raw materials. All the chemicals were purchased from Hi-Media, Mumbai, India, and used as-obtained without any further modifications. The solutions of the metal nitrate salts and citric acid in desired proportions were prepared separately by using minimum amounts of deionized water and mixed in 1:1 molar ratio to form an aqueous solution. Detailed synthesis process of the nanopowders by sol–gel autocombustion method was given in our earlier work [8].

The crystal structures of the as-prepared Ni–Zn–Mn ferrite nanoparticles were analyzed by X-ray powder diffraction technique (Rigaku D/max-250) with  $\text{Cu K}\alpha$  radiation ( $\lambda = 1.5406 \text{ \AA}$ ) in the  $2\theta$  range from  $20^\circ$  to  $70^\circ$ . Thermogravimetric analyses (TGA) were performed on the samples with a heating rate of  $5^\circ\text{C}/\text{min}$  from room temperature up to  $850^\circ\text{C}$  using a Material Analysis and Characterization TG–DTA system. The size and morphology of the ferrite nanoparticles were characterized using TEM (The Tecnai G2 F20 operated at 300 kV). The magnetic properties of the nanoparticles were measured by VSM (Lakeshore-7400) at room temperature in the magnetic field range of  $\pm 11 \text{ kOe}$ .

## 3 Results and discussion

### 3.1 X-ray diffraction analysis

The X-ray diffraction patterns of all the samples of Ni–Zn–Mn ferrite nanoparticles along with crystallite sizes are shown in Fig. 1. All the patterns of the samples can be indexed with the  $2\theta$  values of (Ni, Zn)  $\text{Fe}_2\text{O}_4$  (JCPDS card No. 08-0234) corresponding to the crystal planes of 220, 311, 222, 400, 422, 511 and 440 with no additional peaks, thus indicating the formation of single-phase spinel (ferrite) crystal structures.

Since the intensity levels and background noise at the base level of the patterns are to be considered as measures for degree of crystallinity, it can be inferred from the peaks of the observed patterns that the Ni–Zn–Mn samples are fully crystalline with only little variations in broadening of the peaks, which could be attributed to crystallite sizes apart from the variations in chemical compositions and their corresponding site occupations of the cations present in the system. Also, it can be said that the substitution of Mn in  $\text{Ni}_{0.4}\text{Zn}_{0.6-x}\text{Mn}_x\text{Fe}_2\text{O}_4$  for the full range of substitutions from  $x = 0.00$  to 0.25 completely enters the lattice without leaving any traces of raw materials used.

#### 3.1.1 Crystallite size

Average crystallite size ( $D_p$ ) of the samples in each case was calculated from the broadening of the respective high-intensity best fitting 311 peak using the Scherrer equation,  $D_p = 0.9\lambda/(\beta \cos \theta)$  [9], where  $\lambda$  is the X-ray wavelength ( $1.5406 \text{ \AA}$ ) and  $\beta$  is the broadening of the peak at angle  $\theta$ . The  $\beta$  can be obtained from FWHM of the experimental

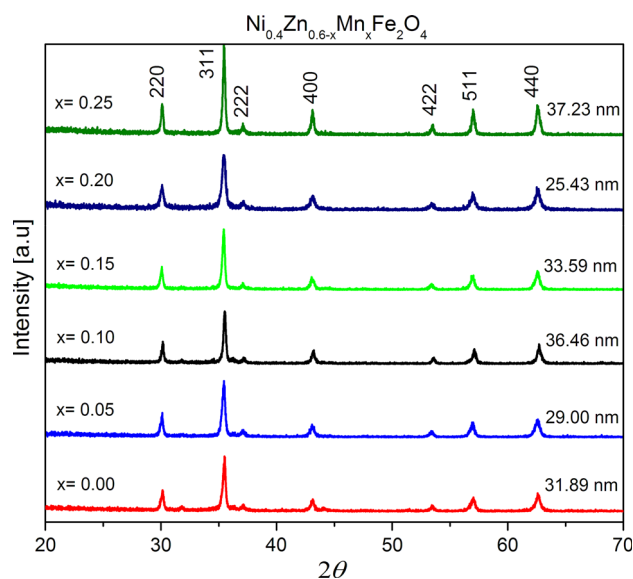


**Fig. 1** XRD patterns of  $\text{Ni}_{0.4}\text{Zn}_{0.6-x}\text{Mn}_x\text{Fe}_2\text{O}_4$  ferrite nanoparticles

profile. For the estimations, the peaks have been considered as Gaussian/Voigt in shape and were best fitted accordingly. Typical Gaussian fit for the sample with  $x = 0.05$  is shown in Fig. 2.

The estimated crystallite size for each of the samples is included at the corresponding pattern itself in the Fig. 1. Further, in order to understand the effect of Mn substitution on the crystalline and structural behavior of Ni–Zn ferrites, the variation of the estimated average crystallite size as a function of Mn concentration for the Ni–Zn–Mn ferrite nanoparticles is shown in Fig. 3.

Though the synthesis conditions were the same for all the samples, the crystallite size was found to be different for different samples and thus the observed variations in crystallite size could be attributed to variations in chemical composition.

### 3.1.2 Lattice constant

Based on the XRD peak central positions obtained from the best fits of all the peaks, the lattice constant was measured in each case. Then, linear plots of the measured lattice parameter versus Nelson–Riley function [10] were drawn and extrapolated the lines to normal incident angle of the X-rays, where all errors vanish, to obtain the experimental lattice parameter. The variation of the estimated values of the lattice constant for the  $\text{Ni}_{0.4}\text{Zn}_{0.6-x}\text{Mn}_x\text{Fe}_2\text{O}_4$  system as a function of Mn concentration is shown in Fig. 4. The lattice constant has been observed to decrease for smaller concentrations of Mn up to  $x = 0.15$ , and thereafter, it increased continuously as the Mn concentration was increased.

The lattice constant of the bulk  $\text{Ni}_{0.4}\text{Zn}_{0.6}\text{Fe}_2\text{O}_4$  prepared by conventional ceramic technique was reported to be  $\approx 8.405 \text{ \AA}$  [11]. As can be observed, the estimated lattice constant of this sample, synthesized by sol–gel autocombustion method, is less than the value of its bulk

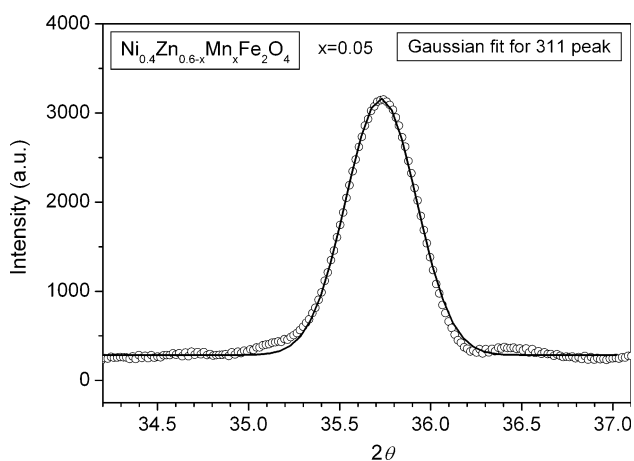


**Fig. 2** Typical Gaussian fit for  $x = 0.05$  of  $\text{Ni}_{0.4}\text{Zn}_{0.6-x}\text{Mn}_x\text{Fe}_2\text{O}_4$

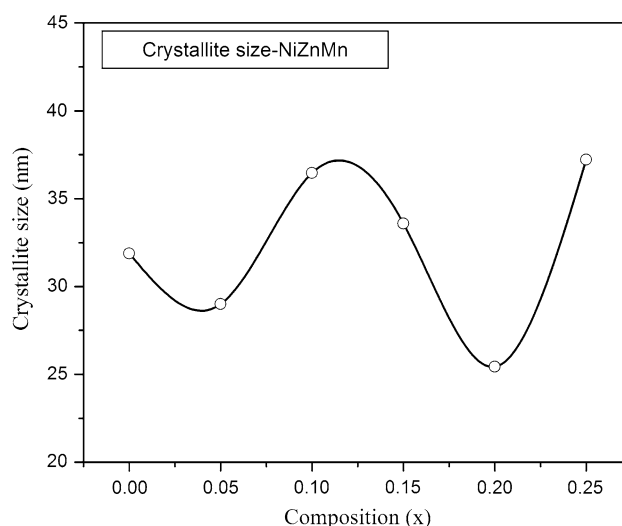


**Fig. 3** Variation of crystallite size as a function of Mn concentration ( $x$ ) for  $\text{Ni}_{0.4}\text{Zn}_{0.6-x}\text{Mn}_x\text{Fe}_2\text{O}_4$

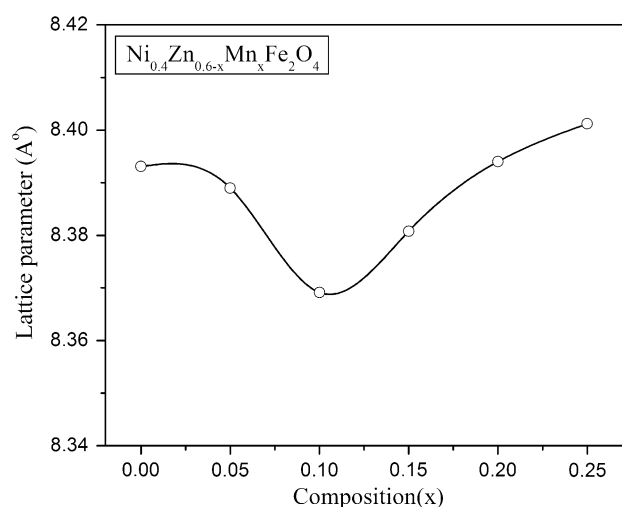


**Fig. 4** Variation of lattice constant as a function of Mn concentration ( $x$ ) for  $\text{Ni}_{0.4}\text{Zn}_{0.6-x}\text{Mn}_x\text{Fe}_2\text{O}_4$  ferrite nanoparticles

counterpart. Further, the observed lattice constants of all the samples in this study seem to have recorded lesser values similar to the undoped Ni–Zn ferrite. Deviations in lattice constants of the nanoparticles from their bulk samples were reported earlier in many works. In some reports, there were enhanced lattices in case of nanoparticles, and the same were attributed to interface structure with a large volume fraction [12]; whereas in others, it was suggested that the decrease in lattice constant could be due to increased degree of inversion [13]. As the inversion increases, the relatively larger  $\text{Zn}^{2+}$  ions in the nanoparticle systems would migrate to B-sites from their conventionally preferred A-sites and comfortably occupy the larger octahedral interstices compared to the smaller tetrahedral interstices. In such case, the  $\text{Zn}^{2+}$  ions need not

necessarily have to push the octahedron around it to expand the lattice. If the  $Zn^{2+}$  ions were in A-sites, they were normally assumed to push the tetrahedron around them and contribute to expand the lattice.

Another probable reason for decrease in lattice constant in ultrafine particles could be the high surface energy and surface tension. This results in a tendency to shrink the lattice which causes reduced lattice constants [14]. The observed deviations in lattice constant in the present study resulting in lower values as the particle size becomes smaller are attributed to the increased degree of inversion, more surface energy and tension-related shrinking of the lattice.

### 3.2 Particle size and morphology

The obtained nanoparticles were partly spherical and partly polyhedron in shape, as observed by typical TEM images shown in Fig. 5a–d. The TEM images of the Fig. 5a, b correspond to the  $x = 0.00$  sample, while the Fig. 5c, d represent sample with  $x = 0.05$  Mn concentration.

The Figures (a) and (c) are taken from a larger view, and those of (b) and (d) are from a closer view. Though the nanoparticles are agglomerated, the figures reveal that the particles are apparently uniform in size and the distribution is also appeared to be narrow. The mean particles size for both the samples was estimated by taking into account the dimensions of about 50–60 particles for each sample and applying the data to log-normal distribution. The mean particle size for  $x = 0.00$  sample was found to be  $30.01 \pm 0.34$  nm, and for the  $x = 0.05$  sample, it was estimated to be  $28.54 \pm 0.33$  nm. These values are in good agreement with the crystallite sizes estimated from Scherrer equation using XRD data for the same samples at 31.89 and 29.0 nm, respectively.

### 3.3 Thermal analysis

Figures 6a, b shows the TG–DTA curves of basic Ni–Zn ferrite nanoparticles ( $x = 0.00$ ) and typical Mn-substituted Ni–Zn ferrite nanoparticles ( $x = 0.10$ ), respectively. The TGA curve of  $x = 0.00$  sample is characterized by two

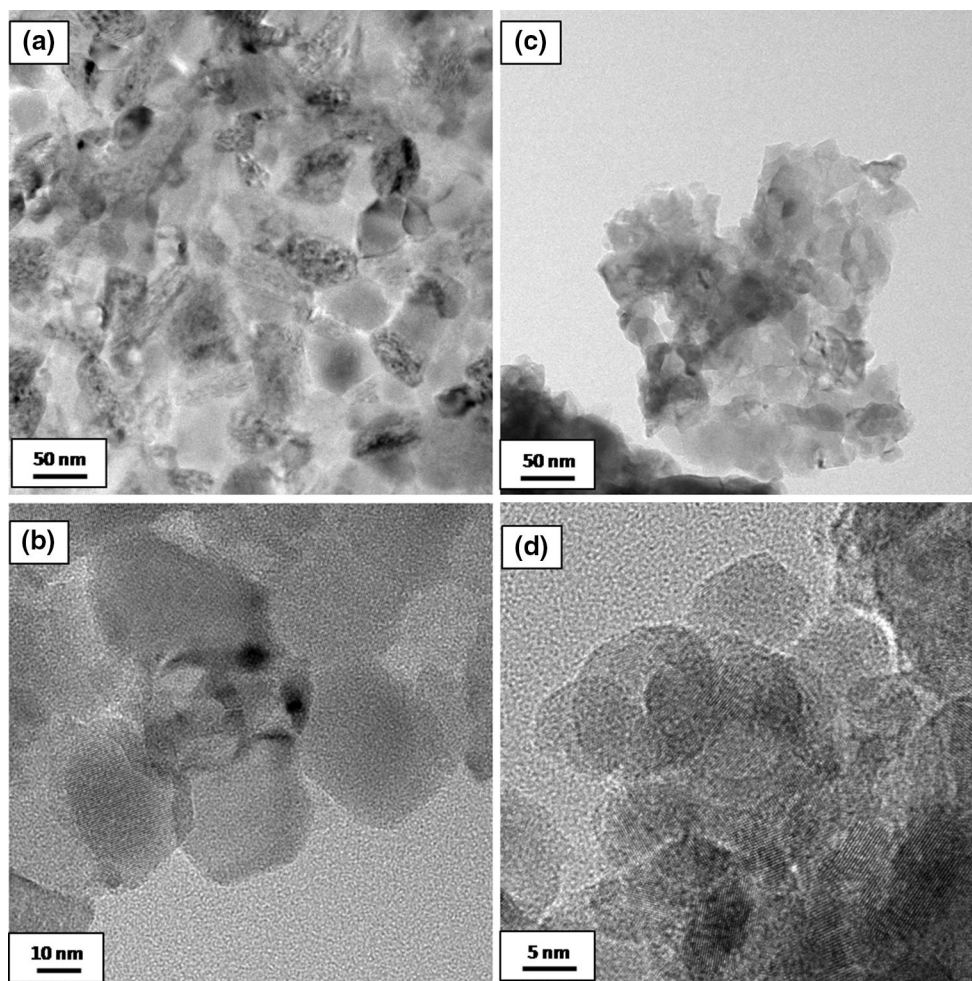


**Fig. 5** Typical TEM images of  $Ni_{0.4}Zn_{0.6-x}Mn_xFe_2O_4$  ( $x = 0.05$ ) ferrite nanoparticles

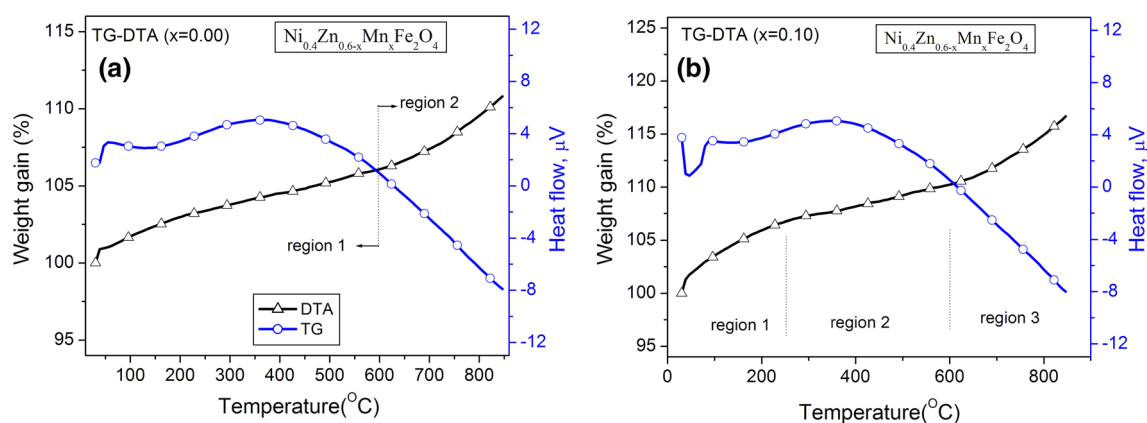


**Fig. 6** **a** TG–DTA curves of as-burnt  $\text{Ni}_{0.4}\text{Zn}_{0.6-x}\text{Mn}_x\text{Fe}_2\text{O}_4$  ( $x = 0.00$ ) ferrite nanoparticles; **b** TG–DTA curves of as-burnt  $\text{Ni}_{0.4}\text{Zn}_{0.6-x}\text{Mn}_x\text{Fe}_2\text{O}_4$  ( $x = 0.10$ ) ferrite nanoparticles

stages for weight change in the temperature ranges of 25–600 and 600–850 °C, whereas the curve of  $x = 0.10$  sample displayed three stages of weight change in the temperature regions of 25–300, 300–600 and 600–850 °C. Interestingly, in both the samples, the weight is marginally increased by about 11% for  $x = 0.00$  sample and 16% for  $x = 0.10$  sample.

The TG–DTA measurements in the present study were carried out on as-burnt samples by the sol–gel autocombustion method, but not during the synthesis. Though it is well known that the decomposition temperatures for the ferrite compound lie around 175 °C, the sample temperatures are observed to go up to approximately 500 °C during the self-propagating combustion process [15]. Thus, the residual nitrates and organic matter, if any are expected to burnt out completely during the combustion reaction itself. However, in the ultrafine regime, the synthesized ferrite nanoparticles may have sizeable irregularly shaped or distorted atoms with broken exchange bonds on their surfaces [16]. Though the presence of these surface imperfections is quantitatively very small compared to the spinel ferrite phase, they are easily prone to either oxidation/reduction chemical reactions or adsorb water molecules in substantial quantity to result in weight modifications of the sample. In the light of these arguments, the observed TG–DTA curves were seen for providing valuable information pertaining to the changes imposed by the surface imperfections apart from structural modifications such as crystallization or recrystallization during heating.

The particle size and atomic configuration change when the nanoparticles are exposed to high temperatures since the free energy of these particles is greater than that of their bulk counterparts. A small increase in weight could be attributed to increase in magnetization as a result of changes in cation distribution due to corresponding changes in ionic sizes of the cations residing in different lattice sites. Similar increases in weight due to metastable cation

distribution during heating followed by a possible increase in magnetization have been reported earlier [17, 18]. These observations suggest that the ferrite materials in nanoscale regime experience metastable cation distribution, and subsequent heating of the nanoparticles at elevated temperatures helps them to come back to their normal distribution according to their natural preferences to different crystallographic lattice site in the spinel [19, 20].

In the case of  $x = 0.00$  sample with the absence of Mn for any oxidation, the first region (up to 600 °C) of weight change with an increase of approximately 5% is corresponded largely to the presence of metastable cation distribution at the surface of the ferrite nanoparticles [17]. This rather slow change in weight gain in this region may be partly due to parallel evaporation of surface adsorbed water as well as any residues deposited [21]. And, for the second region from 600 to 800 °C, there observed an increased rate of weight gain (by about 6%), which is attributed mainly to the improved crystallization to reduce the surface imperfections and cation redistribution according to the normal site preferences of the  $\text{Ni}^{2+}$  and  $\text{Zn}^{2+}$  ions with a corresponding increase in magnetization to be presented in the next section. Whereas, in the case of  $x = 0.10$  sample, the complexity is further increased with the presence of Mn ions leading to increased degree of surface imperfections as well as metastable cation distribution. Thus, slightly higher weight gain was observed initially up to 250 °C for this sample. Then, from 250 to 600 °C, the counter effects of the crystallization process in the direction of weight gain and evaporation of surface adsorbed water in the opposite direction of weight loss prevail simultaneously only to confine the net rate of weight gain to about 3% in this region. Thereafter, at temperatures beyond 600 °C, the Mn is known to partly oxidize into  $\text{Mn}^{3+}$  ions [22], which have strong preference for B-sites, and thus, the cation distribution of the ferrite system becomes further complex with the simultaneous

presence of all the four cations (Ni, Mn, Fe and Zn) in both A- and B-sites. Additional weight gains are likely when oxidation processes take place resulting in bringing new atoms into the sample and thus increasing its mass. Thus, the observed rapid increase in weight gain between 600 and 800 °C by about 7% is attributed to oxidation process as well as improved migration of the cations to the sites of their natural preferences resulting in higher magnetization.

### 3.4 Saturation magnetization and coercivity

Room temperature magnetic hysteresis loops, which were recorded using vibrating sample magnetometer, for all the samples of the  $\text{Ni}_{0.4}\text{Zn}_{0.6-x}\text{Mn}_x\text{Fe}_2\text{O}_4$  ferrite nanoparticles in the external magnetic field range of  $\pm 11$  kOe are shown in Fig. 7. It can be inferred from the observed loops that all the samples are magnetically saturated with finite values of coercivity implying that the investigated Ni–Zn–Mn ferrite nanoparticles exhibit ferrimagnetic behavior. The magnetic properties such as saturation magnetization (herein after called as magnetization) and coercivity were extracted from these observed hysteresis loops, and their variations as a function of Mn concentration ( $x$ ) are shown in Fig. 8.

Despite the fact that a diamagnetic Zn is replaced with ferromagnetic Mn at each step of substitution in the ferrite system of  $\text{Ni}_{0.4}\text{Zn}_{0.6-x}\text{Mn}_x\text{Fe}_2\text{O}_4$  nanoparticles, the magnetization of the system has been observed to have a sinusoidal variation with Mn concentration ( $x$ ). That means the substitution of Mn in the given nano-sized Ni–Zn–Mn ferrite system does not cause a straightforward replacement of Zn simply by occupying the vacant sites arising out of displaced Zn ions. Instead, the incorporation of Mn in the system seems to have profound influence not only on the site preferences of other cations in the system but also in bringing about modifications in its own site preferences.

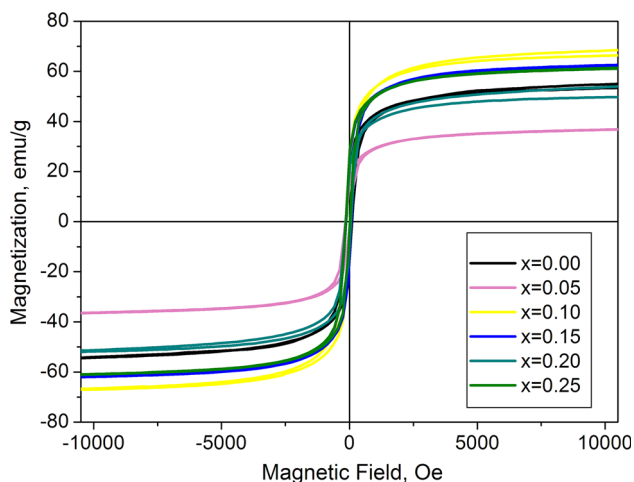


**Fig. 7** Magnetic hysteresis loops of  $\text{Ni}_{0.4}\text{Zn}_{0.6-x}\text{Mn}_x\text{Fe}_2\text{O}_4$  ferrite nanoparticles

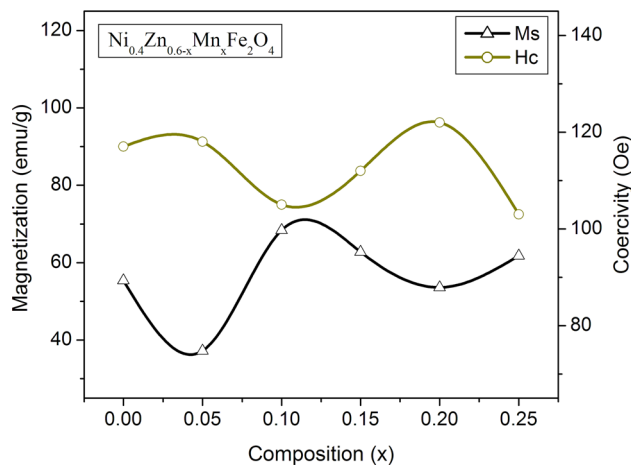


**Fig. 8** Variations of magnetization and coercivity with Mn concentration ( $x$ ) for  $\text{Ni}_{0.4}\text{Zn}_{0.6-x}\text{Mn}_x\text{Fe}_2\text{O}_4$  ferrite nanoparticles

Moreover, since the modified cationic preferences for occupation of sublattice sites in nanoparticles systems are size dependent, the observed values of magnetization for different samples in the given Ni–Zn–Mn ferrite nanoparticles seem to have influenced by the particle sizes of the respective samples. Particularly, when the size scales of the ferrite materials come down to few tens of nanometers, this kind of increased dependence of the magnetization on particle size and cation redistribution as against the bulk cationic preferences is expected. Similar results of magnetic properties arising from particle size-dependent deviations in mean degree of inversion in nanoscale ferrites have been reported in many instances [23, 24]. Therefore, in order to accurately explain the variation of magnetization with Mn substitution in the given ferrite system, it needs to be thoroughly examined the roles of size dependence and inversion degree on the magnetic behavior of these materials.

Further, as can be seen from the Fig. 8, the observed behaviors of the magnetization and the coercivity of the  $\text{Ni}_{0.4}\text{Zn}_{0.6-x}\text{Mn}_x\text{Fe}_2\text{O}_4$  nanoparticles are opposite to each other. The coercivity of the magnetic material strongly depends upon the domain structure, particle size and anisotropy of the material [25]. In the nanoregime, the size distribution of the particles becomes even more important as the surface-to-volume ratio is so large and the surfaces of the ultrafine particles contribute significantly to the magnetic anisotropy in the form of shape anisotropy apart from the magnetocrystalline anisotropy. Thus, for arriving at a specific conclusion on what really affected the magnetization and coercivity behavior in the present Ni–Zn–Mn ferrite nanoparticles, it is felt necessary to find out whether we can obtain any relation for explaining the influence of particle size and cation distribution on the magnetic behavior of these materials.

In spinel ferrites, the magnetic cations residing in different sublattices (A- and B-sites) align to have opposite magnetic moments according to the Neel's molecular field theory [26]. So, the magnetic moment per formula unit ( $n_B$ ) in Bohr magneton ( $\mu_B$ ) comes from the expression  $n_B(x) = M_B(x) - M_A(x)$ , where  $M_B$  and  $M_A$  are the magnetic moments of B-sites and A-sites in Bohr magneton.

The experimental magnetic moment per formula unit in Bohr magneton was estimated for all the samples using the molecular weight of the respective sample, and its value of the saturation magnetization ( $M_s$ ) was obtained from the magnetic hysteresis loops, by the relation [27]

$$n_B = \text{Mol. Wt.} \times M_s / 5585$$

where the numerical term 5585 is the magnetic factor.

As discussed earlier, the crystallite sizes of all the samples were estimated by applying the Scherrer equation to the most intense peak (311) of the X-ray diffractogram. It follows from the above, the dependence of the crystallite size on the magnetic moment for all the samples is shown in Fig. 9. It can be clearly seen from the figure that the trend lines of crystallite size and the magnetic moment go hand in hand for the whole range of Mn substitutions in  $\text{Ni}_{0.4}\text{Zn}_{0.6-x}\text{Mn}_x\text{Fe}_2\text{O}_4$  nanoparticles. Similar results of size-dependent magnetic properties have been widely reported in the literature. Rajendran et al. [16] reported a steady increase in magnetization in  $\text{CoFe}_2\text{O}_4$  nanocrystallites when the crystallite size is increased. They expressed that the net magnetic moment could be reduced in ultrafine particles for the simple reason that the sample has significantly large surface-to-volume ratio. In such case, it is likely that a large proportion of the metal ions exist on the structurally distorted particle surfaces, wherein, the magnetic contributions from the bond lengths and bond angles

in nanoparticles systems would be much different from their bulk to give reduced magnetic moments. Hartridge et al. [28] in their study of magnetite nanopowders observed a crystallite size threshold between 9 and 20 nm, below which the surface area to volume ratios are large enough to induce electric field gradients around the iron sites within the crystallite, leading to a collapse of the magnetic ordering while resulting in inferior magnetic performance.

Caizer and Stefanescu [29] reported in Ni–Zn ferrites a monotonous increase in the specific saturation magnetization with the increase in the nanocrystallites' mean diameter, yet the values obtained for the saturation magnetization are sensibly lower than those of the bulk ferrite. They attributed this behavior to the surface effects which appear as a result of the finite size of nanocrystallites and lead to a non-collinearity of the magnetic moments at the nanocrystallite surface. And, they further expressed that the effects are getting more intense as the mean size of the nanocrystallites is getting smaller and the surface/volume ratio is increasing. The observations of  $\text{Ni}_{0.35}\text{Zn}_{0.65}\text{Fe}_2\text{O}_4$  nanocrystallites in the size range of 20.3–37.9 nm reported by Caizer and Stefanescu [29] appear close to the ones presented in our study of  $\text{Ni}_{0.4}\text{Zn}_{0.6-x}\text{Mn}_x\text{Fe}_2\text{O}_4$  nanoparticles and our samples too have formed with crystallites in the similar size range from 25.43 to 37.23 nm. Thus, similar explanations of structurally distorted surfaces with broken exchange bonds and surface spin canting would suit to explain the observed synchronizing variations of crystallite size and magnetic moment of our  $\text{Ni}_{0.4}\text{Zn}_{0.6-x}\text{Mn}_x\text{Fe}_2\text{O}_4$  ferrite nanoparticles presented above.

## 4 Conclusions

X-ray diffraction analyses on the synthesized samples of Ni–Zn–Mn ferrite nanoparticles confirm the formation of highly crystalline single-phase spinel structures with cubic symmetry. The crystallite sizes of the samples were estimated using Scherrer equation and were found to be varying in the range from 25.43 to 37.23 nm. Besides, particle sizes were also measured from the obtained TEM images of some samples, and they were found to be in good agreement with the crystallite sizes of the respective samples obtained from the Scherrer formulae. The TG–DTA curves of the Mn-substituted sample records a slight additional weight gain due to oxidation of the Mn and thereby formation of new ions. The extracted saturation magnetization (54–68 emu/g) and coercivity (103–122 Oe) values of the synthesized Ni–Zn–Mn ferrite nanoparticles from the measured M–H loops have shown improved magnetic properties at the Mn substitutions of  $x = 0.10$  and 0.15 concentrations. Thus, the Mn-substituted Ni–Zn

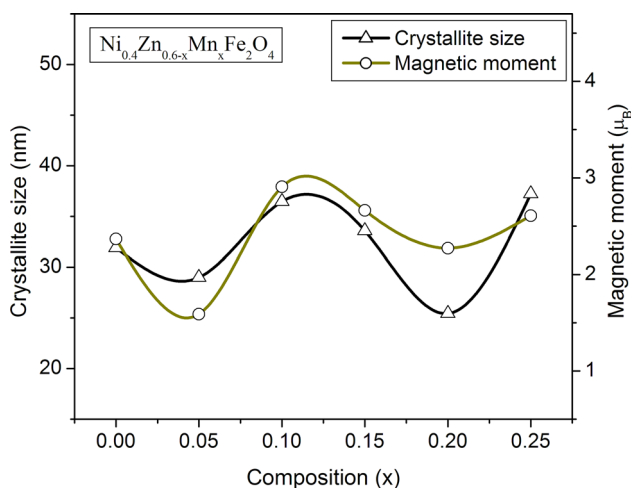


**Fig. 9** Variations of the crystallite size and the magnetic moment as a function of Mn concentration ( $x$ ) for  $\text{Ni}_{0.4}\text{Zn}_{0.6-x}\text{Mn}_x\text{Fe}_2\text{O}_4$  ferrite nanoparticles

ferrites with good structural and magnetic properties find themselves useful to be developed as core materials for high-frequency applications.

**Acknowledgements** The authors thank DST-PURSE for extending financial support during the course of the investigations.

## References

1. E.C. Snelling, *Soft ferrites, properties and applications*, 2nd edn. (Butterworths, London, 1988)
2. A. Verma, R. Chatterjee, *J. Magn. Magn. Mater.* **306**, 318–320 (2006)
3. S. Prijic, G. Sersa, *Radiol. Oncol.* **45**, 1–16 (2011)
4. M.J. Iqbal, M.N. Ashiq, P. Hernandez-Gomez, J.M. Munoz, *J. Magn. Magn. Mater.* **320**, 881–886 (2007)
5. S. Zahi, *J. Electromagn. Anal. Appl.* **2**, 56–62 (2010)
6. D.O. Yener, H. Giesche, *J. Am. Soc.* **84**, 1987–1995 (2001)
7. A. Dias, R.L. Moreira, *Mater. Lett.* **39**, 69–76 (1999)
8. S. Ramesh, B. Dhanalakshmi, B. Chandra Sekhar, P.S.V. Subba Rao, B. Parvatheeswara Rao, *Ceram. Int.* **42**, 9591–9598 (2016)
9. B.D. Cullity, *Elements of X-ray Diffraction* (Adison-Wesley, London, 1959), p. 261
10. R. Das, S. Sarkar, *Curr. Sci.* **109**(4), 25 (2015)
11. L.K. Leung, B.J. Evans, A.H. Morrish, *Phys. Rev. B* **8**, 29–43 (1973)
12. L. Wang, F.S. Li, *Chin. Phys.* **9**, 685–688 (2000)
13. B.P. Rao, C.-O. Kim, C.G. Kim, I. Dumitru, L. Spinu, O.F. Caltun, *IEEE Trans. Magn.* **42**, 2858–2860 (2006)
14. B.T. Naughton, D.R. Clarke, *J. Am. Ceram. Soc.* **90**, 3541–3546 (2007)
15. A. Sutka, G. Mezinskis, *Front. Mater. Sci.* **6**, 128–141 (2012)
16. M. Rajendran, R.C. Pullar, A.K. Bhattacharya, D. Das, S.N. Chintalapudi, C.K. Majumdar, *J. Magn. Magn. Mater.* **232**, 71–83 (2001)
17. L. Nalbandiana, A. Delimitis, V.T. Zaspalis, E.A. Deliyanni, D.N. Bakoyannakis, E.N. Peleka, *Microporous Mesoporous Mater.* **114**, 465–473 (2008)
18. Z. Yue, J. Zhou, L. Li, H. Zhang, Z. Gui, *J. Magn. Magn. Mater.* **208**, 55–60 (2000)
19. A.K. Singh, A.K. Singh, T.C. Goel, R.G. Mendiratta, *J. Magn. Magn. Mater.* **281**, 276–280 (2004)
20. P.S. Anil Kumar, J.J. Shrotri, S.D. Kulkarni, C.E. Deshpande, S.K. Date, *Mater. Lett.* **27**, 293–296 (1996)
21. L. Yu, S. Cao, Y. Liu, J. Wang, C. Jing, J. Zhang, *J. Magn. Magn. Mater.* **301**, 100–106 (2006)
22. R. Gerber, G. Elbinger, *J. Phys. C Solid State Phys.* **3**, 1363–1375 (1970)
23. V. Sepelak, U. Steinike, D. Chr, S. Uecker, K.D. Becker Wibmann, *J. Solid State Chem.* **135**, 52–58 (1998)
24. L. Wang, F.S. Li, *J. Magn. Magn. Mater.* **223**, 233–237 (2001)
25. S. Chikazumi, S. Charap, *Physics of Magnetism* (Wiley, New York, 1964), p. 153
26. H. Li, H. Wu, G. Xiao, *Powder Technol.* **198**, 157–166 (2010)
27. J. Smit, *Magnetic Properties of Material, Inter-University Electronics Series*, vol. 13 (McGraw-Hill, New York, 1971), p. 29
28. A. Hartridge, A.K. Bhattacharya, M. Sengupta, C.K. Majumdar, D. Das, S.N. Chintalapudi, *J. Magn. Magn. Mater.* **176**, 89–92 (1997)
29. C. Caizer, M. Stefanescu, *Phys. B* **327**, 129–134 (2003)